This article has been accepted for publication in a future issue of this journal, but has not been fully edited. Content may change prior to final publication. Citation information: DOI 10.1109/TAP.2020.2978280, IEEE Transactions on Antennas and Propagation

X wave radiator implemented with 3D printed metamaterials

Nikolaos Chiotellis[1], Shiyu Zhang[2], Yiannis C. Vardaxoglou[2], and Anthony Grbic[1]

***Abstract*—A radiator is presented, capable of generating paraxial X waves over a 50% fractional bandwidth ($7.5 - 12.5$ GHz) in its radiative near field. X waves are localized pulses formed by the superposition of Bessel beams with a common cone angle. Quasiconformal transformation optics, a 2D variant of transformation optics, is employed to find the inhomogeneous, isotropic dielectric constant profile needed to convert the radiation of a monopole into a paraxial Bessel beam. An impedance matching layer is applied to reduce reflections at the air-dielectric interface of the device. The transformation and impedance matching regions are implemented using rotationally symmetric metamaterial unit cells that yield a spatially varying effective dielectric constant. The resulting design is fabricated through 3D printing, by combining parts made from three low-loss dielectric filaments. The device is experimentally measured, and shows good agreement with simulations. Its ability to generate paraxial X waves when excited by a broadband pulse is verified.**

***Index Terms*—metamaterials, effective dielectric constant, Bessel beam, nondiffracting beams, radiative near field, 3D printing**

I. Introduction

LOCALIZED waves have received significant attention by researchers in recent years, especially since the introduction of Bessel beams [1], [2]. Bessel beams are exact, superluminal solutions to the Helmholtz equation that do not diffract as they propagate. They can be seen as the result of the interference of all plane waves forming a common angle, called the cone angle, with the propagation axis. Although ideal Bessel beams require infinite energy, truncated Bessel beams are practically realizable. Such beams maintain their nondiffractive properties within a finite range of distances.

X waves are one class of Bessel pulses [3]. They are formed by a frequency spectrum of Bessel beams possessing a common cone angle. X waves are appealing because they propagate without suffering from diffraction (spatial spreading) or dispersion (temporal spreading) within their nondiffracting range. These properties make X waves prime candidates for use in imaging [4], tissue characterization [5], communications [6], nondestructive evaluation of materials [7], and focusing [8].

Submitted for review on .... Published on.... This work was supported by the Air Force Office of Scientific Research (Grant No. FA9550-15-1-0101), the Office of Naval Research under Grant No. N00014-18-1-2536, and the UK EPSRC grand challenge SYMETA (www.symeta.co.uk).

[1]The authors are with the Electrical Engineering and Computer Science Department, University of Michigan, Ann Arbor, MI 48109, USA (e-mail: agrbic@umich.edu).

[2]The authors are with the Wolfson School of Mechanical, Electrical and Manufacturing Engineering, Loughborough University, Loughborough, Leicestershire, UK.

X waves are difficult to generate at microwave frequencies, which partially explains the lack of relevant practical demonstrations in literature. A device generating X waves should exhibit little or no dispersion (dependence of cone angle on frequency) over an appreciable bandwidth. The cost of broadband sources is also an impeding factor. Should these hurdles be overcome, there is high potential for microwave X waves in heating [9], medicine [10], microscopy [11], high power electromagnetic pulses [12], or ground penetrating radar applications [13].

A device capable of generating X waves at microwave frequencies was presented recently by the authors [14], [15]. Based on geometrical optics, the device converts the radiation from an electrically small monopole into Bessel beams with nearly constant cone angle between 18 and 30 GHz. In earlier research, a parabolic dish was used to verify the superluminality of X Waves [16]. A radial waveguide loaded with radiating slots [17] as well as leaky wave antennas [18], [19] have also been suggested as potential ways to excite X Waves at microwave and millimeter wave frequencies. However, these devices exhibit more pronounced dispersion. Here, a new device is presented, that can emit paraxial Bessel beams and X waves between 7.5 and 12.5 GHz. It is designed using quasiconformal transformation optics (QCTO) [20], [21], implemented with metamaterials, and fabricated through 3D printing. Preliminary results on the design methodology were reported in [22], [23].

Transformation electromagnetics provides arbitrary control of electromagnetic fields through control of constitutive material parameters (permittivity and permeability) as functions of space (inhomogeneity) and direction (anisotropy) [24], [25]. QCTO is a 2D method of manipulating fields that only requires control of permittivity as a function of space [20]. Permeability, which is more difficult to control, is constant, while both permittivity and permeability are isotropic. This technique is used here to design a 3D device that possesses rotational symmetry about the $\widehat{z}$-axis, and as a result can be reduced to a 2D problem [21].

An exponentially tapered impedance matching layer (IML) is added to the permittivity profile obtained from QCTO to reduce reflections at the interface with air [26]. The combined permittivity profile is implemented using rotationally symmetric metamaterial unit cells which are homogenized and modeled with effective permittivities [27]. The resulting device is fabricated through 3D printing, which is an additive manufacturing technique [28]. In this work, the device is partitioned into three parts, and three filaments of different permittivity values are used to realize the required permittivity

This article has been accepted for publication in a future issue of this journal, but has not been fully edited. Content may change prior to final publication. Citation information: DOI 10.1109/TAP.2020.2978280, IEEE Transactions on Antennas and Propagation

profile of the parts. The parts are later assembled to form the device. Metamaterial structures requiring multiple filaments can be potentially fabricated in a single run [29].

The design of the tranformation region based on QCTO, together with the design of the IML, is presented in Sec. II. The validity of the design is verified by comparing the electric field generated by this structure to that of an ideal Bessel aperture, computed using a full wave solver. The metamaterial implementation of the radiator using rotationally symmetric unit cells is outlined in Sec. III, along with the corresponding simulation results. In Sec. IV, the fabrication procedure and the challenges associated with it are explained. Measurement results from a fabricated prototype are also given, showing good agreement to those expected from simulation. Sec. V showcases the device's ability to generate X waves in its radiative near field when excited with a uniform spectrum pulse between 7.5 and 12.5 GHz. Finally, Sec. VI presents concluding remarks.

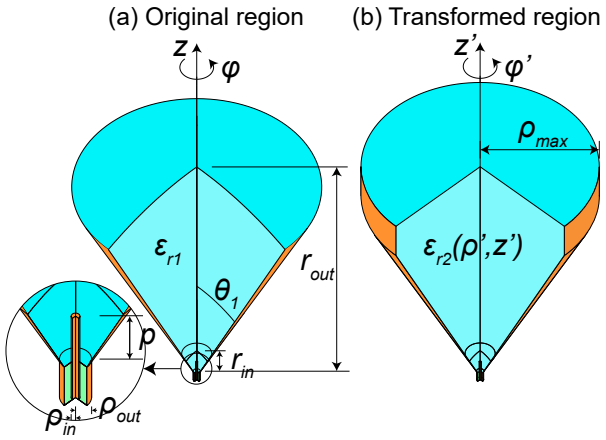

Fig. 1. (a) The original region, comprising a coaxially fed monopole radiating in a conical region of homogeneous permittivity ϵ_{r1}, and bounded by a spherical surface at $r = r_{out}$. (b) The transformed region, utilizing the same feeding mechanism, having an inhomogeneous permittivity $\epsilon_{r2}(\rho', z')$ and bounded by a flat surface at $z' = r_{out}$.

II. Design of X Wave Radiator

Consider an electrically small monopole radiating in a conical region with apex angle θ_1 and relative permittivity ϵ_{r1}, as shown in Fig. 1(a). The monopole is situated at the apex of the cone, which is bounded by perfect electric conductor (PEC) shown in orange. The monopole is formed by extending the inner conductor of the coaxial cable feeding it by length p, which, together with θ_1 and ϵ_{r1}, controls the input impedance of the device. The coaxial cable has inner radius ρ_{in} and outer radius ρ_{out}, as shown in the inset of Fig. 1(a). The generated electric field has $\widehat{\rho}$ and $\widehat{z}$ components, whereas the magnetic field only has a $\widehat{\phi}$ component. This field will be converted into a TM Bessel beam.

The equiphase surfaces of the fields emitted by the monopole will be approximately spheres centered at the origin. Two such surfaces are chosen for the analysis that follows, one having radius r_{in} and one having radius r_{out} (see Fig. 1(a)). The region between the two spheres constitutes the original region and is expressed in terms of (ρ, ϕ, z) cylindrical coordinates.

The transformed region using (ρ', ϕ', z') coordinates is shown in Fig. 1(b). The parameters for the coaxial cable and monopole comprising the feed are kept the same. This region possesses a flat surface at $z' = r_{out}$, and is truncated to a maximum radius of ρ_{max}. The truncation ensures that the permittivity profile obtained from QCTO at a later step will not contain unrealizably small permittivity values. The apex angle is still θ_1, but the region in Fig. 1(b) has an inhomogeneous relative permittivity $\epsilon_{r2}(\rho', z')$.

The two regions presented in Fig. 1(a) and (b) should behave similarly, meaning that the flat surface in the transformed region should constitute an equiphase surface. Because of the problem's cylindrical symmetry about the $\widehat{z}$-axis, this results in the generation of a paraxial Bessel beam. Moreover, this symmetry means that these 3D regions can be treated as 2D surfaces, and analyzed using QCTO [21].

The purpose of the transformation is to simply convert the spherical wavefronts into flat ones, the interference of which

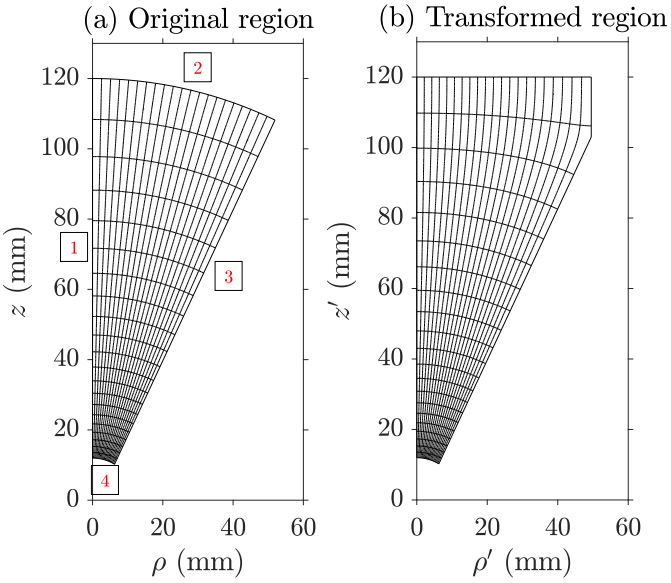

Fig. 2. (a) Original, and (b) transformed regions in 2D, used in QCTO.

creates the Bessel beam. The chosen transformation is not a radical one by design. A simple transformation means that the range of values in $\epsilon_{r2}(\rho', z')$ is small. This leads to a transformed region that can be realized with commercially available filaments suitable for 3D printing. More exotic transformations (such as an exponential or hyperbolic transition) require more extreme values of $\epsilon_{r2}(\rho', z')$, which may not be compatible with the chosen manufacturing technique.

Fig. 2(a) and (b) show the original and transformed regions in 2D, respectively. In these figures, the mesh for the two regions is also shown. The mesh is obtained by solving Laplace's equation in each region, subject to appropriate boundary conditions [21]. First, Neumann boundary conditions are applied on edges 1 and 3, and Dirichlet boundary conditions on edges 2 and 4. The edge numbers are shown in red. After solving Laplace's equation, a contour plot of the solution's amplitude yields the isocentric curves in Fig. 2(a).

This article has been accepted for publication in a future issue of this journal, but has not been fully edited. Content may change prior to final publication. Citation information: DOI 10.1109/TAP.2020.2978280, IEEE Transactions on Antennas and Propagation

TABLE I
VALUES OF DESIGN VARIABLES

Design variable	Value
ρ_{in}	0.455 mm
ρ_{out}	1.485 mm
p	11.3 mm
θ_1	25°
r_{in}	12 mm
r_{out}	120 mm
ρ_{max}	49.5 mm
t	9 mm
ϵ_{r1}	5.4
ϵ_{r2}	2.90 - 7.36

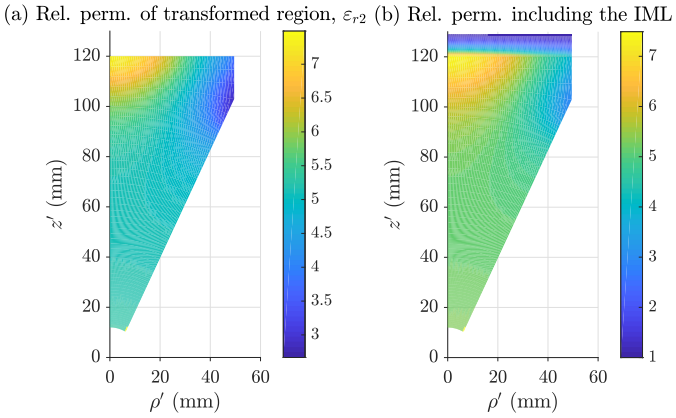

Fig. 3. The relative permittivity profile of the transformed region (a) before, and (b) after the application of the IML.

Then the straight, spokes-like curves in Fig. 2(a) are obtained by applying Dirichlet boundary condition on edges 1 and 3, and Neumann boundary conditions on edges 2 and 4. Similar boundary conditions are applied on the transformed region.

Using the design equations originally presented in [20] and in a more compact way in [21], the relative permittivity profile of the transformed region is calculated as

$$\epsilon_{r2}(\rho', z') = \frac{\epsilon_{r1}}{|\det(\mathbf{J}(\rho', z'))|}, \tag{1}$$

where

$$\mathbf{J}(\rho', z') = \begin{bmatrix} \frac{\partial \rho'}{\partial \rho} & \frac{\partial \rho'}{\partial z} \\ \frac{\partial z'}{\partial \rho} & \frac{\partial z'}{\partial z} \end{bmatrix} \tag{2}$$

is the Jacobian matrix of the transformation from the original region shown in Fig. 2(a) to the transformed region of Fig. 2(b).

The resulting permittivity profile, shown in Fig. 3(a), is smooth, and agrees with intuition from gradient index optics, where rays bend towards regions of higher permittivity. The relative permittivity of the original region, ϵ_{r1}, was chosen so that the relative permittivity of the transformed region is nondispersive and falls within a range that can be realized through 3D printing. The overall dimensions were also decided on based upon fabrication capabilities and constraints. Table I summarizes the design variables and their values.

The next step in the design process is to apply an impedance matching layer (IML) of thickness t to the transformed region to minimize reflections caused by the high contrast of

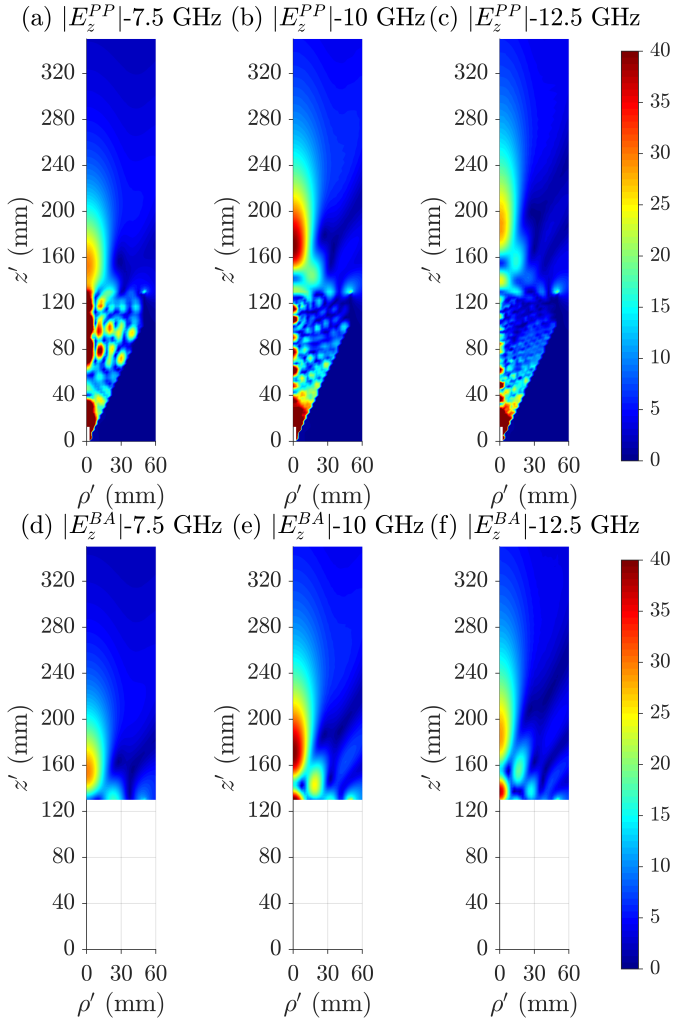

Fig. 4. $|E_z|$ (in V/m) emitted by the permittivity profile of Fig. 3(b) at (a) 7.5, (b) 10, and (c) 12.5 GHz, respectively. (d-f) $|E_z|$ emitted by an ideal Bessel aperture at the same three frequencies for comparison.

refractive indices at the flat interface (assuming the device is surrounded by air). An exponential taper was selected for the IML instead of a quarter wavelength transformer [30]. The IML is thicker, but provides an impedance match over a broader bandwidth. Its dielectric constant is

$$\epsilon_{r,IML}(\rho', z') = \epsilon_{r2}(\rho', r_{out}) e^{-\ln(\epsilon_{r2}(\rho', r_{out}))(z' - r_{out})/t}, \tag{3}$$

where $\epsilon_{r2}(\rho', r_{out})$ is the dielectric constant at the interface, as calculated from QCTO [30].

The final dielectric constant profile, comprising the transformed region and the IML, is shown in 2D in Fig. 3(b). The radiator possessing this permittivity profile was simulated at three frequencies, 7.5, 10, and 12.5 GHz, in the axially symmetric solver of COMSOL Multiplhysics. The amplitude of the longitudinal ($\widehat{z}'$-directed) electric fields in the region over the radiator are shown in Fig. 4(a-c) when a voltage of 1 V excites the coaxial cable. The cone angles of the emitted beams are $\theta = 18°$, $14°$, and $11°$, respectively. The nondiffracting range of the beams, calculated as $\rho_{max}\cot\theta$, is 152, 199, and 255 mm from the aperture, respectively. In

This article has been accepted for publication in a future issue of this journal, but has not been fully edited. Content may change prior to final publication. Citation information: DOI 10.1109/TAP.2020.2978280, IEEE Transactions on Antennas and Propagation

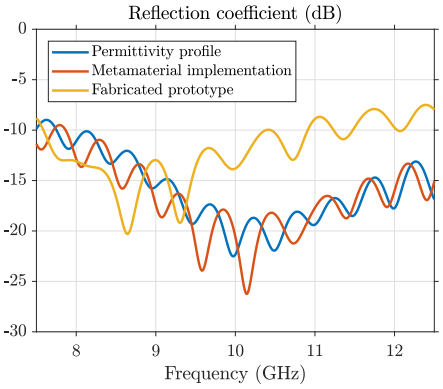

Fig. 5. The reflection coefficient of the radiator having the permittivity profile of Fig. 3(b) (blue), the reflection coefficient of the radiator implemented with metamaterial unit cells (orange), and the reflection coefficient of the fabricated prototype (Fig. 12) (yellow).

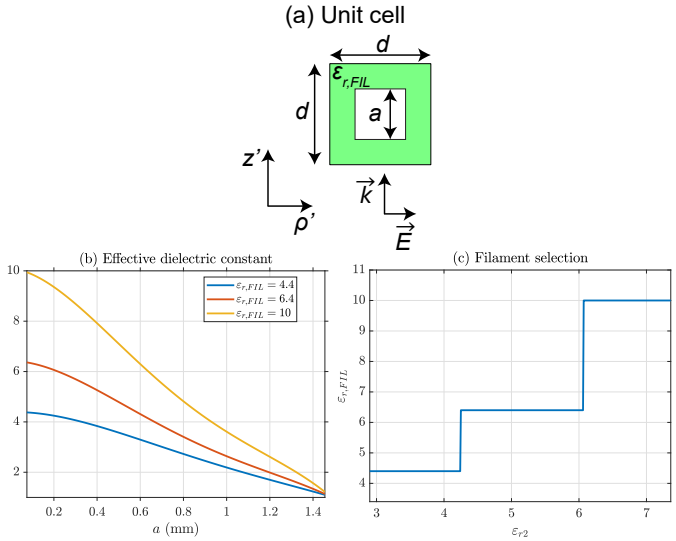

Fig. 6. (a) Unit cell used to implement the permittivity profile obtained from QCTO. (b) The effective dielectric constant of this unit cell as a function of parameter a for different values of $\epsilon_{r,FIL}$. (c) The model developed to determine which filament should be used to implement a required effective dielectric constant.

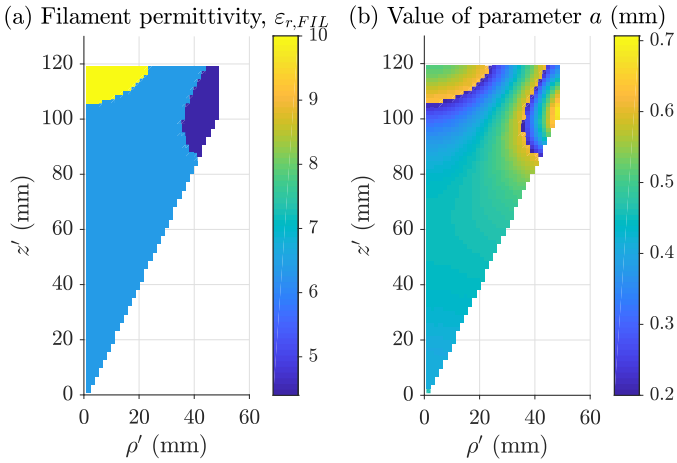

Fig. 7. (a) Using the permittivity profile of Fig. 2(a) and the model of Fig. 6(c), the filament to be used at each point of the radiator is determined. (b) Knowing which filament will be used, the value of parameter a is determined using the appropriate homogenization curve in Fig. 6(b).

order to achieve a smaller cone angle, which would result in a larger nondiffracting range, an electrically larger aperture is required. A larger aperture can produce a beam with narrower beamwidth, allowing the peak to approach broadside.

For comparison, the field generated from ideal Bessel apertures with these cone angles is investigated. The aperture has tangential electric field profile given by

$$E_\rho(\rho') \propto J_1(k_0 \sin\theta \rho'), \quad \rho' \leq \rho_{max}, \tag{4}$$

where k_0 is the free space wavenumber and is placed at the same z' as the aperture of the radiator ($z' = r_{out} + t = 129$ mm). The resulting $\widehat{z}'$-directed electric field amplitudes are shown in Fig. 4(d-f) at the same three frequencies. Although not identical, the field profiles appear quite similar, and agree in terms of range.

The reflection coefficient of the radiator including the IML is shown in Fig. 5 in blue. The shape of this curve is dictated largely by the reflection coefficient of the monopole, while the rest of the radiator contributes the small scale ripple. A broadband match is observed.

III. Metamaterial Implementation

The permittivity profile of Fig. 3(a) is implemented using the 2D metamaterial unit cell shown in Fig. 6(a), which was studied in [27]. It consists of a square of side d made from a material with dielectric constant $\epsilon_{r,FIL}$, from which a square of side a has been removed. When swept about the $\widehat{z}'$-axis, it results in circular channels with square cross sections. By changing the dielectric constant of the material, $\epsilon_{r,FIL}$, and parameter a, a large range of effective dielectric constants can be achieved with dimensions suitable for 3D printing.

The materials used should exhibit good electromagnetic properties (namely, be low-loss) and possess a controlled dielectric constant. PREPERM® filaments offered by PREMIX [31] fulfill these criteria and are used here. Specifically, filaments with $\epsilon_{r,FIL} = 4.4$, 6.4, and 10 are used. Their loss tangent is $\tan\delta = 0.004$.

The effective dielectric constant is found by simulating the unit cell of Fig. 6(a) in COMSOL. The unit cell size is set to $d = 1.5$ mm. The effective dielectric constant of the unit cell as a function of parameter a is plotted in Fig. 6(b) for the three filaments.

This unit cell has a uniaxial permittivity tensor with equal values in the $\widehat{\rho}'$- and $\widehat{z}'$- directions and a different one in the $\widehat{\phi}'$-direction. Since the fields emitted by the monopole are always polarized in plane with the unit cell, only the $\widehat{\rho}'$ and $\widehat{z}'$-directed permittivity is relevant.

The model of Fig. 6(c) is used to decide which filament should be used depending on the effective dielectric constant needed. It is based on fabrication constraints imposed by 3D printing on the value of parameter a. This parameter must be kept between 0.2 and 0.7 mm. For example, to achieve $\varepsilon_{r2} = 5$ at a specific point of the radiator, the $\varepsilon_{r,FIL} = 6.4$ filament should be used according to Fig. 6(c). From the

This article has been accepted for publication in a future issue of this journal, but has not been fully edited. Content may change prior to final publication. Citation information: DOI 10.1109/TAP.2020.2978280, IEEE Transactions on Antennas and Propagation

homogenization curves of Fig. 6(b), $a = 0.46$ mm is the appropriate value to achieve $\varepsilon_{r2} = 5$ with the the $\varepsilon_{r,FIL} = 6.4$ filament. In this way, the filament permittivity, $\varepsilon_{r,FIL}$, and parameter a were determined for the entire device. Their values are given in Fig. 7(a) and (b), respectively.

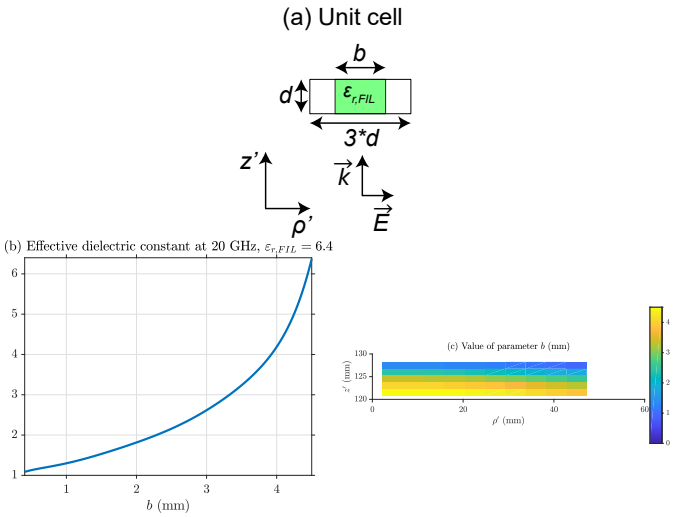

Fig. 8. (a) Unit cell used to implement the IML portion of Fig. 3(b). (b) Effective dielectric constant of this unit cell (using $\varepsilon_{r,FIL} = 6.4$) as a function of parameter b through simulation in COMSOL. (c) Distribution of parameter b in the IML, based on this model and Fig. 3(b).

Applying the same procedure for the IML would result in very large values for a (close to d, even if a filament with $\varepsilon_{r,FIL} = 3$ were to be used), which could not be fabricated through 3D printing. As a result, a different approach is developed to implement the IML.

Specifically, the unit cell of Fig. 8(a) is used to implement the IML, which may be considered as a simplified version of the unit cells in [29]. It consists of a rectangle with dimensions $b \times d$, made of filament with dielectric constant $\varepsilon_{r,IML} = 6.4$. The unit cell size is $3d \times d$. By changing parameter b, the effective permittivity of the unit cell can be tuned, as shown in Fig. 8(b). Implementing the IML portion of the permittivity profile (Fig. 3(b)) using the curve in Fig. 8(b) results in the distribution for parameter b shown in Fig. 8(c).

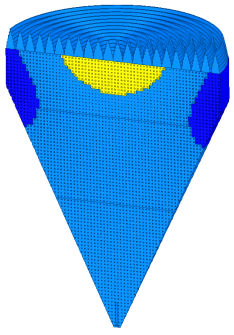

Fig. 9. The rotationally symmetric metamaterial implementation of the QCTO and IML regions of the radiator. Dark blue: $\varepsilon_{r,FIL} = 4.4$, light blue: $\varepsilon_{r,FIL} = \varepsilon_{r,IML} = 6.4$, yellow: $\varepsilon_{r,FIL} = 10$.

The design resulting from the metamaterial implementation of the QCTO and IML regions is presented in Fig. 9. Each

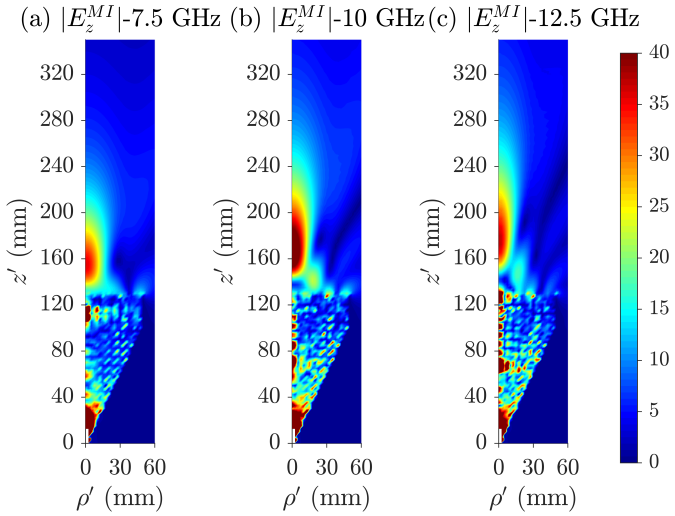

Fig. 10. $|E_z|$ (in V/m) obtained by simulating the radiator that is implemented with metamaterial unit cells at (a) 7.5, (b) 10, and (c) 12.5 GHz, respectively.

filament is represented by a different color: dark blue - $\varepsilon_{r,FIL} = 4.4$, light blue - $\varepsilon_{r,FIL} = 6.4$, yellow - $\varepsilon_{r,FIL} = 10$. This radiator design is simulated in the axially symmetric solver of COMSOL at the same three frequencies: 7.5, 10, and 12.5 GHz. The results, shown in Fig. 10, agree with the ones obtained using the inhomogeneous permittivity profile (Fig. 4(a-c)), justifying the metamaterial design procedure. The reflection coefficient of the metamaterial implementation is also obtained through COMSOL simulations, and is presented in Fig. 5 in orange.

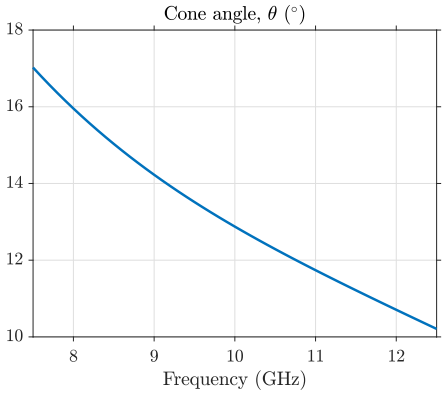

Fig. 11. Cone angle of the radiator implemented using metamaterial unit cells as a function of frequency.

In simulation, the cone angle of the Bessel beam generated by the radiator is also investigated. Specifically, Fig. 11 presents the cone angle as a function of frequency between 7.5 and 12.5 GHz. Any practical device will have a dependence of cone angle on frequency. The radiator presented in this paper exhibits a variation of 7° between 7.5 and 12.5 GHz, or 0.14° per % bandwidth. Bulkier radiators exhibit a smaller variation (2° between 18 and 30 GHz or 0.04° per % bandwidth [15]), while planar ones exhibit larger variation (12° between 18 and 20 GHz, or 1.14° per % bandwidth [19]). A larger cone

This article has been accepted for publication in a future issue of this journal, but has not been fully edited. Content may change prior to final publication. Citation information: DOI 10.1109/TAP.2020.2978280, IEEE Transactions on Antennas and Propagation

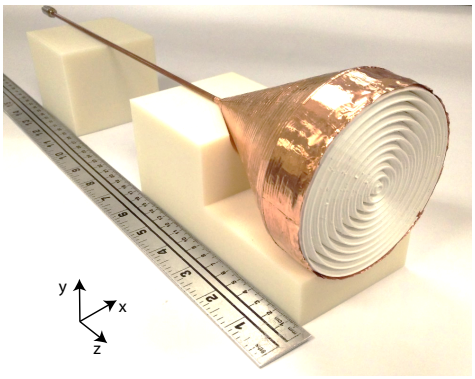

Fig. 12. Fabricated prototype of the metamaterial implementation of the radiator, obtained through 3D printing.

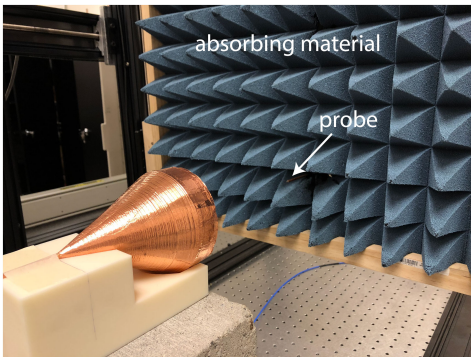

Fig. 13. Measurement setup used to scan the $\widehat{z}'$-directed electric field emitted by the radiator.

angle dispersion degrades the confinement of the X wave pulse emitted by the radiator, since different frequency components will travel at different velocities ($v \propto 1/\cos\theta$) [17].

IV. Measurement Results

The metamaterial radiator was fabricated through 3D printing, using PREPERM® filaments. Each part of the transformed region was manufactured using the appropriate filament (Fig. 7(a)) and distribution of parameter a (Fig. 7(b)). The IML was also 3D printed using $\epsilon_{r,FIL} = 6.4$, and the distribution of parameter b shown in Fig. 8(c). A cross section of the design is shown in Fig. 9.

The $\epsilon_{r,FIL} = 4.4$ parts were printed using the Makerbot Replicator 2X 3D printer, while the $\epsilon_{r,FIL} = 6.4$ and $\epsilon_{r,FIL} = 10$ parts were printed using the Voxel8 3D printer. All parts were then glued together using acetone. The monopole feeding the device was made from RG402 coaxial cable, and copper foil (3M®1126) was applied to the exterior of the device to form the conductive cladding. The fabricated prototype is shown in Fig. 12.

The fabrication of the parts, as well as their assembly into one structure proved quite challenging:

- Due to the complexity and size of the $\epsilon_{r,FIL} = 6.4$ part, its printing had to be further subdivided into four smaller printing jobs, as shown in Fig. 9.
- Some of the parts exhibited a bow due to the variation of temperature within the 3D printing chamber. A combination of sanding and lathing of the affected surfaces was necessary to flatten the parts so that they would be flush upon assembly.
- Great care was taken to minimize the air gaps between the parts. However, due to the tight fit between some of the parts and the hardness of the material, some air gaps between parts could not be avoided.
- Inserting the electrically small monopole vertically into the 3D printed region was challenging.

The longitudinal ($\widehat{z}'$-directed) electric field was measured in the region over the radiator (1601 frequency points between 5 and 15 GHz). An electrically-small monopole surrounded by absorber and attached to a 3D translation stage was used as a probe. Both the radiator and the probe were connected to a vector network analyzer that was used to measure the signal transmitted between the two. A picture of the measurement setup is shown in Fig. 13. A schematic of the area in which the fields are measured is shown in Fig. 14.

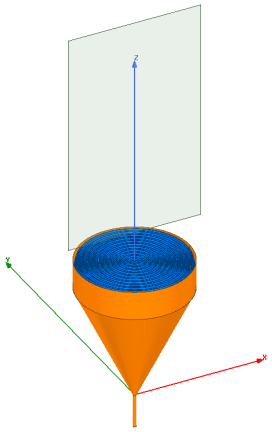

Fig. 14. The plane on which the longitudinal electric field is measured in the region over the radiator.

The normalized fields along the $(\widehat{x}' - \widehat{z}')$ plane, simulated using COMSOL, are shown at 7.5, 10, and 12.5 GHz in Fig. 15(a), (c), and (e), respectively. The experimentally measured fields along this plane at the same three frequencies are shown in Fig. 15(b), (d), and (f). The measurement results agree well with those from simulation. Small discrepancies start to appear at higher frequencies, where the unintenional features of the 3D printing process become more prominent and begin to degrade the radiator's performance. The nondiffracting range extends to $z' = 0.28$ m at 7.5 GHz and to $z' = 0.38$ m at 12.5 GHz.

The reflection coefficient of the fabricated prototype is shown in Fig. 5 in yellow. The discrepancy between the measured reflection coefficient and the one expected from simulation is attributed to the assembly process of the prototype. Significant effort was placed in minimizing the air gaps between parts, which can cause reflections. However, it was not possible to completely eliminate them.

This article has been accepted for publication in a future issue of this journal, but has not been fully edited. Content may change prior to final publication. Citation information: DOI 10.1109/TAP.2020.2978280, IEEE Transactions on Antennas and Propagation

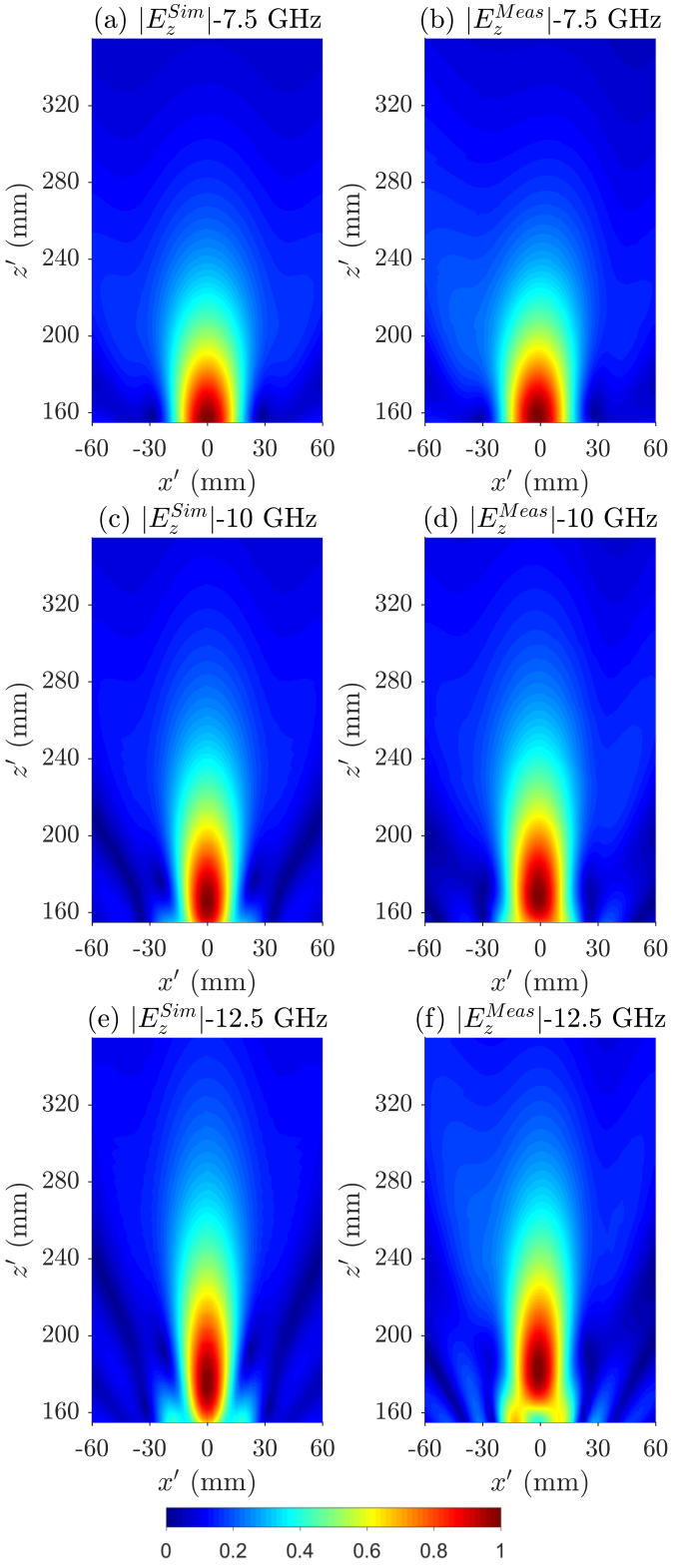

Fig. 15. The longitudinal ($\hat{z}'$-directed) electric field in the region over the radiator: (a) simulation and (b) measurement results at 7.5 GHz, (c) simulation and (d) measurement results at 10 GHz, (e) simulation and (f) measurement results at 12.5 GHz.

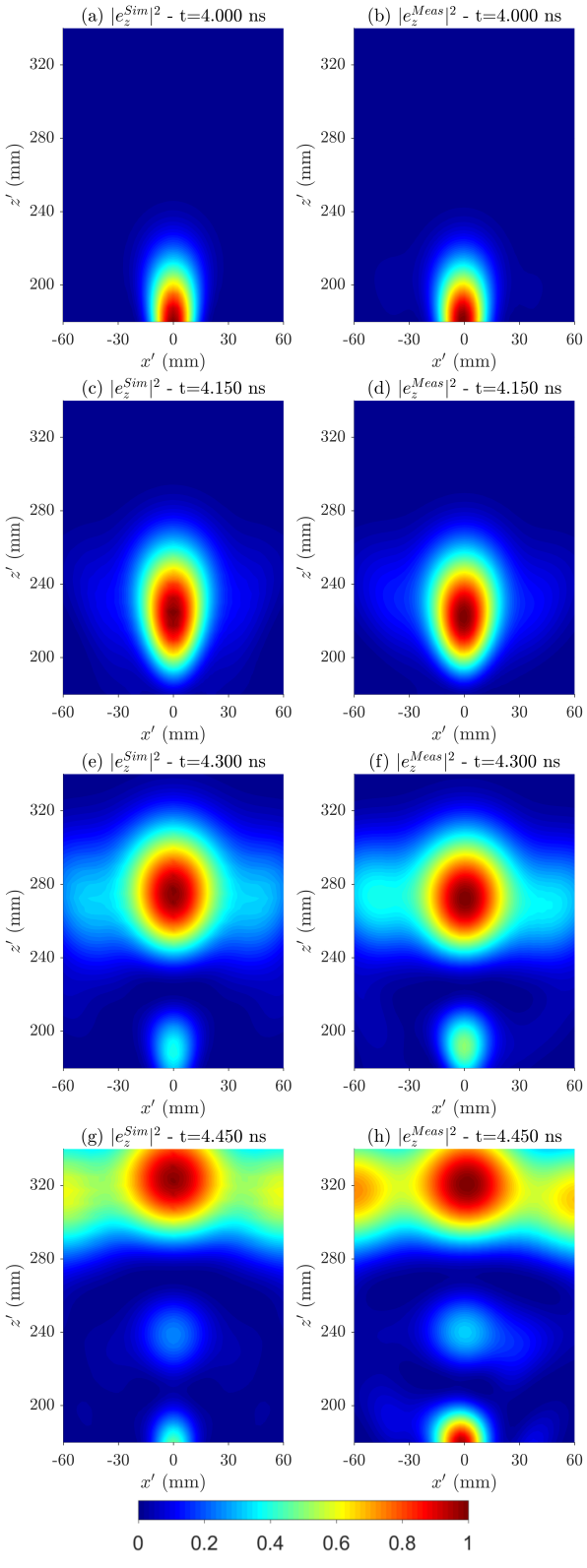

Fig. 16. The intensity of the longitudinal ($\hat{z}'$-directed) electric field in the region over the radiator as a function of space and time when excited with a uniform spectrum pulse (7.5 – 12.5 GHz): using (a) simulation and (b) measurement results at 4 ns, (c) simulation and (d) measurement results at 4.15 ns, (e) simulation and (f) measurement results at 4.3 ns, (g) simulation and (h) measurement results at 4.45 ns.

This article has been accepted for publication in a future issue of this journal, but has not been fully edited. Content may change prior to final publication. Citation information: DOI 10.1109/TAP.2020.2978280, IEEE Transactions on Antennas and Propagation

V. Generation of X waves

X waves are pulses consisting of a spectrum of monochromatic Bessel beams exhibiting the same cone angle, θ. Assuming a uniform spectrum, the waveform (longitudinal electric field in this case) of an ideal X wave is given as a function of time, t, and cylindrical coordinates, (ρ, z), by [1]

$$E_z(\rho, z, t) = \int_{\omega_{min}}^{\omega_{max}} J_0(\omega \sin\theta \rho / c_0) e^{j\omega(t - \cos\theta z/c_0)} d\omega, \quad (5)$$

where J_0 is the zeroth order Bessel function of the first kind, ω is the angular frequency, and c_0 is the speed of light.

The time domain response of the radiator to a uniform spectrum pulse can be calculated as

$$E_z(x', z', t) = \sum_{\omega_i = 2\pi 7.5\text{GHz}}^{2\pi 12.5\text{GHz}} E_z(x', z', \omega_i) e^{j\omega_i t}, \quad (6)$$

where $E_z(x', z', \omega_i)$ is the simulated or measured value of E_z, which depends on spatial coordinates and frequency. The longitudinal electric field produced by the radiator, E_z, is that of an apodized Bessel beam.

Fig. 16(a), (c), (e), and (g) present the intensity of the X wave produced by the radiator in simulation. Fig. 16(b), (d), (f), and (h) present the intensity of the measured X wave produced by the radiator. Each plot has been normalized between 0 and 1 for ease of comparison. Close agreement is observed between the X wave based on simulation data and the one based on measured data. The measured X wave exhibits more prominent secondary lobes and tail. However, the shapes of the two pulses largely agree with each other.

VI. Conclusion

In this paper, a Bessel beam radiator using a metamaterial region to bend the rays of an electric monopole was presented. The design procedure, based on quasiconformal transformation optics, was outlined, and verified through simulation results. A design procedure based on metamaterial synthesis was employed to implement the device using rotationally symmetric unit cells. Simulation results confirmed the validity of this approach. Experimental results from a fabricated prototype were presented, showing good agreement with those obtained through simulation. Using simulation and experimental data, it was shown that the device is capable of generating X waves in its radiative near field.

The progress reported here, combined with other recent advancements in the field of X waves, pave the way for many exciting applications. From imaging to communications, and from heating to high power electromagnetic pulses, X waves are prime candidates for applications that requires highly localized microwave pulses.

Finally, 3D printing has already been established as a manufacturing technique for lenses over the past decade. This work demonstrates how 3D printing can also be employed to fabricate interesting near field devices that are directly fed. The incorporation of the feed in the printed part contributes to the reduction of the size of the device. Future advancements in available filament materials and the capabilities of 3D printers will solidify the ubiquitousness of 3D printing in electromagnetic design.

References

[1] H. E. Hernández-Figueroa, M. Zamboni-Rached, and E. Recami, *Localized waves*. John Wiley & Sons, 2007, vol. 194.

[2] J. Durnin, "Exact solutions for nondiffracting beams. I. The scalar theory," *JOSA A*, vol. 4, no. 4, pp. 651–654, 1987.

[3] J.-Y. Lu and J. F. Greenleaf, "Nondiffracting X waves-exact solutions to free-space scalar wave equation and their finite aperture realizations," *IEEE Transactions on Ultrasonics, Ferroelectrics, and Frequency Control*, vol. 39, no. 1, pp. 19–31, 1992.

[4] ——, "Ultrasonic nondiffracting transducer for medical imaging," *IEEE Transactions on Ultrasonics, Ferroelectrics, and Frequency Control*, vol. 37, no. 5, pp. 438–447, 1990.

[5] J. Y. Lu and J. F. Greenleaf, "Evaluation of a nondiffracting transducer for tissue characterization," in *1990 IEEE Symposium on Ultrasonics*, vol. 2, 1990, pp. 795–798.

[6] J.-Y. Lu and S. He, "Optical X wave communications," *Optics Communications*, vol. 161, no. 4, pp. 187–192, 1999.

[7] J.-Y. Lu and J. F. Greenleaf, "Producing deep depth of field and depth-independent resolution in NDE with limited diffraction beams," *Ultrasonic Imaging*, vol. 15, no. 2, pp. 134–149, 1993.

[8] A. M. Shaarawi, I. M. Besieris, and T. M. Said, "Temporal focusing by use of composite X waves," *JOSA A*, vol. 20, no. 8, pp. 1658–1665, 2003.

[9] J. M. Osepchuk, "A history of microwave heating applications," *IEEE Transactions on Microwave Theory and Techniques*, vol. 32, no. 9, pp. 1200–1224, 1984.

[10] F. Sterzer, "Microwave medical devices," *IEEE Microwave Magazine*, vol. 3, no. 1, pp. 65–70, 2002.

[11] C. Gao, T. Wei, F. Duewer, Y. Lu, and X.-D. Xiang, "High spatial resolution quantitative microwave impedance microscopy by a scanning tip microwave near-field microscope," *Applied Physics Letters*, vol. 71, no. 13, pp. 1872–1874, 1997.

[12] M. G. Backstrom and K. G. Lovstrand, "Susceptibility of electronic systems to high-power microwaves: Summary of test experience," *IEEE Transactions on Electromagnetic Compatibility*, vol. 46, no. 3, pp. 396–403, 2004.

[13] D. J. Daniels, "Ground penetrating radar," *Encyclopedia of RF and Microwave Engineering*, 2005.

[14] N. Chiotellis and A. Grbic, "A broadband, Bessel beam radiator," in *2016 IEEE International Symposium on Antennas and Propagation (APSURSI)*, 2016, pp. 873–874.

[15] N. Chiotellis, V. Mendez, S. M. Rudolph, and A. Grbic, "Experimental demonstration of highly localized pulses (X waves) at microwave frequencies," *Physical Review B*, vol. 97, no. 8, p. 085136, 2018.

[16] D. Mugnai, A. Ranfagni, and R. Ruggeri, "Observation of superluminal behaviors in wave propagation," *Physical Review Letters*, vol. 84, no. 21, p. 4830, 2000.

[17] W. Fuscaldo, S. C. Pavone, G. Valerio, A. Galli, M. Albani, and M. Ettorre, "Analysis of limited-diffractive and limited-dispersive X-waves generated by finite radial waveguides," *Journal of Applied Physics*, vol. 119, no. 19, p. 194903, 2016.

[18] W. Fuscaldo, D. Comite, A. Boesso, P. Baccarelli, P. Burghignoli, and A. Galli, "Focusing leaky waves: A class of electromagnetic localized waves with complex spectra," *Physical Review Applied*, vol. 9, p. 054005, May 2018.

[19] D. Comite, W. Fuscaldo, S. Podilchak, V. Gómez-Guillamón Buendía, P. Hilario Re, P. Baccarelli, P. Burghignoli, and A. Galli, "Microwave generation of X-waves by means of a planar leaky-wave antenna," *Applied Physics Letters*, vol. 113, no. 14, p. 144102, 2018.

[20] J. Li and J. B. Pendry, "Hiding under the carpet: a new strategy for cloaking," *Physical Review Letters*, vol. 101, no. 20, p. 203901, 2008.

[21] M. Ebrahimpouri and O. Quevedo-Teruel, "Bespoke lenses based on quasi-conformal transformation optics technique," *IEEE Transactions on Antennas and Propagation*, vol. 65, no. 5, pp. 2256–2264, 2017.

[22] N. Chiotellis and A. Grbic, "Metamaterial Bessel beam radiator," in *2017 IEEE International Symposium on Antennas and Propagation (APSURSI)*, 2017, pp. 1735–1736.

[23] ——, "Metamaterial-based Bessel beam launcher," in *2017 IEEE 11th International Congress on Engineered Materials Platforms for Novel Wave Phenomena (Metamaterials)*, 2017, pp. 55–57.

[24] J. B. Pendry, D. Schurig, and D. R. Smith, "Controlling electromagnetic fields," *Science*, vol. 312, no. 5781, pp. 1780–1782, 2006.

This article has been accepted for publication in a future issue of this journal, but has not been fully edited. Content may change prior to final publication. Citation information: DOI 10.1109/TAP.2020.2978280, IEEE Transactions on Antennas and Propagation

[25] U. Leonhardt, "Optical conformal mapping," *Science*, vol. 312, no. 5781, pp. 1777–1780, 2006.
[26] M. Q. Qi, W. X. Tang, and T. J. Cui, "A broadband Bessel beam launcher using metamaterial lens," *Scientific reports*, vol. 5, 2015.
[27] C. R. Garcia, J. Correa, D. Espalin, J. H. Barton, R. C. Rumpf, R. Wicker, and V. Gonzalez, "3D printing of anisotropic metamaterials," *Progress In Electromagnetics Research*, vol. 34, pp. 75–82, 2012.
[28] R. C. Rumpf, J. Pazos, C. R. Garcia, L. Ochoa, and R. Wicker, "3D printed lattices with spatially variant self-collimation," *Progress in Electromagnetics Research*, vol. 139, pp. 1–14, 2013.
[29] D. Isakov, Q. Lei, F. Castles, C. Stevens, C. Grovenor, and P. Grant, "3D printed anisotropic dielectric composite with meta-material features," *Materials & Design*, vol. 93, pp. 423–430, 2016.
[30] D. M. Pozar, *Microwave Engineering*. John Wiley & Sons, 2012.
[31] *Dielectric Parts for Easy RF-prototyping — PREPERM®*. www.preperm.com/products/stock-shapes/#filaments.